Mon. Not. R. Astron. Soc. **000**, 000–000 (0000) Printed December 18, 2013 (MN LaTeX style file v2.2)

Swirling around filaments: are large-scale structure vortices spinning up dark halos?

C. Laigle[1], C. Pichon[1,2], S. Codis[1], Y. Dubois[1], D. Le Borgne[1], D. Pogosyan[5], J. Devriendt[4], S. Peirani[1], S. Prunet[1], S. Rouberol[1], A. Slyz[3], T. Sousbie[1]

[1] *Institut d'Astrophysique de Paris & UPMC (UMR 7095), 98 bis boulevard Arago, 75014 Paris, France*
[2] *Institute of Astronomy, University of Cambridge, Madingley Road, Cambridge, CB3 0HA, United Kingdom*
[3] *KITP Kohn Hall-4030 University of California Santa Barbara, CA 93106-4030*
[4] *Astrophysics, University of Oxford, Keble Road, Oxford OX1 3RH, United Kingdom*
[5] *Department of Physics, University of Alberta, 11322-89 Avenue, Edmonton, Alberta, T6G 2G7, Canada.*

December 18, 2013

ABSTRACT

The kinematic analysis of dark matter and hydrodynamical simulations suggests that the vorticity in large-scale structure is mostly confined to, and predominantly aligned with their filaments, with an excess of probability of 20 per cent to have the angle between vorticity and filaments direction lower than 60° relative to random orientations. The cross sections of these filaments are typically partitioned into four quadrants with opposite vorticity sign, arising from multiple flows, originating from neighbouring walls. The spins of halos embedded within these filaments are consistently aligned with this vorticity for any halo mass, with a stronger alignment for the most massive structures up to an excess of probability of 165 per cent.

The global geometry of the flow within the cosmic web is therefore qualitatively consistent with a spin acquisition for smaller halos induced by this large-scale coherence, as argued in Codis et al. (2012). In effect, secondary anisotropic infall (originating from the vortex-rich filament within which these lower-mass halos form) dominates the angular momentum budget of these halos. The transition mass from alignment to orthogonality is related to the size of a given multi-flow region with a given polarity. This transition may be reconciled with the standard tidal torque theory if the latter is augmented so as to account for the larger scale anisotropic environment of walls and filaments.

Key words: large-scale structure – galaxies: halos – galaxies: formation – method: numerical.

1 INTRODUCTION

The standard paradigm of galaxy formation addresses the acquisition of spin via the so-called Tidal Torque Theory (TTT Hoyle 1949; Peebles 1969; Doroshkevich 1970; White 1984) for which collapsing protogalaxies acquire their spin because of a misalignment between their inertia tensor and their (local) tidal tensor. There is ample evidence that for massive (quasi linear) clusters, TTT provides a sound theoretical framework in which to describe angular momentum (AM) acquisition during the linear phase of structure formation. Conversely, lighter non-linear structures undergo significant drift within the large-scale tidal field, move some distance away from their original Lagrangian patch (see, e.g. Schaefer 2009, for a review). Over the last 10 years, numerical simulations as well as theoretical consideration (Katz et al. 2003; Birnboim & Dekel 2003; Kereš et al. 2005; Ocvirk et al. 2008) have accumulated evidence that the intricate cosmic web plays a critical role in the process of forming high-redshift galaxies. In the initial phase of galaxy formation, the condition of the intergalactic medium leads to essentially isothermal shocks. Hence cold gas follows closely the cosmic web while radiating away the thermal energy gained by the extraction of kinetic energy every time its trajectory dictates the formation of a shock.

The dynamical relevance of the anisotropy of the cosmic web for galaxy formation may have been partially underestimated given the small mass involved (in contrast to the mass in peaks). Indeed, spherical collapse and Press-Schechter theory have been quite successful at explaining the mass function of galaxies (Press & Schechter 1974), while TTT accounts reasonably well for the amplitude of the global spin parameters measured in simulations (Schaefer 2009). On the other hand, the morphology of galaxies, arguably a secondary feature, is controlled at high redshift by the AM (see for instance Dubois et al. 2012) and is very likely driven by later infall of AM-rich gas. In turn, the critical ingredient must therefore be the anisotropy of such infall, driven by its dynamics within the cosmic web, which differ significantly (via the hitherto mentioned shocks) from that of the dark matter, since cold flows advect the angular momentum they acquired as they formed during the early phase of large-scale structure formation. A paradigm for the acquisition of disc angular momentum via filamentary flows was recently proposed by Pichon et al. (2011) which found a closer connection between the 3D geometry and dynamics of the neighbouring cosmic web and the properties of embedded dark halos than originally suggested by the standard hierarchical formation paradigm (see also Prieto et al. 2013; Stewart et al. 2013). At these scales, in the surrounding asymmetric gravitational patch gas streams out from the neighbouring voids, towards their encompassing filaments where it shocks, until the cold flows are swallowed by the forming galaxy, advecting their newly acquired angular momentum (Kimm et al. 2011; Tillson et al. 2012). While the gas is streamed out of the walls towards their surrounding filaments it winds up and forms the first generation of galaxies with a spin parallel to the filaments (Aragón-Calvo et al. 2007; Hahn et al. 2007; Paz et al. 2008; Zhang et al. 2009; Codis et al. 2012; Libeskind et al. 2013, see also Aubert et al. 2004; Bailin & Steinmetz 2005, for earlier indication of anisotropic inflows). These authors explored the link between dark matter (DM) halos' spins and the cosmic web to quantify this alignment. They detected a redshift dependent mass transition $M_{\rm crit}$, varying with the scale (or equivalently with the hierarchical level of the cosmic structure in which the halo is embedded, see Aragón-Calvo 2013). Codis et al. (2012) interpreted the signal in terms of large-scale cosmic flows: high-mass halos have their spins perpendicular to the filament because they are the results of major mergers (see also Peirani et al. 2004); low-mass halos are not the products of merger and acquire their mass by accretion, which explain that their spins are parallel to the filament. Danovich et al. (2011) also studied the feeding of massive galaxies at high redshift through cosmic streams using the Horizon-MareNostrum simulation (Ocvirk et al. 2008) and found that galaxies are fed by one dominant stream with a tendency to be fed by three major streams; these streams tend to be co-planars and there are hints of AM exchange at the interphase between the stream and the disk. All these investigations suggest the existence of an additional mechanism other than the vanilla TTT, affecting first low-mass halos: mass accretion in an anisotropic, multi-flow environment.

Tempel et al. (2013) and Zhang et al. (2013) have recently found evidence of such alignment in the SDSS (an orthogonality for S0 galaxies and a weak alignment for late type spirals).

The detailed origin of this correlation, while not strictly speaking surprising, as well as its measured dependence on mass, has not yet been fully understood. The spin of the dark halo represents, in essence, the vortical motion of the matter and as such can be expected to reflect the vorticity in the surrounding protogalactic patch of a forming halo. Indeed, to understand this trend, Libeskind et al. (2013) has argued that the local *vorticity* was more relevant than the original tidal field in setting up the direction of dark halo spins. They have explored the link between vorticity in halo environment and the origin of halos spin and found a strong alignment between both. Vorticity tends to be perpendicular to the axis along wich material is collapsing fastest. A natural telltale of such process would be a significant large-scale vorticity generation *in* the multiflow regions corresponding to the interior of filaments. Recently, Wang et al. (2013) revisited this description by introducing three invariants of the velocity gradient tensor and concluded that vorticity generation is highly correlated with large scale structure before and after shell-crossing, in a way which depends on the flow morphology. The TTT successfully traces the origin of the angular momentum of a halo to the quasi-nonlinear stage of halo collapse, however vorticity per se arises only after shell crossing in multistreaming regions and requires the look inside such regions. Pioneering study of Pichon & Bernardeau (1999) theoretically demonstrated that in the simplest pancake-like multistream collapse the level of the vorticity generated is of the order of Hubble constant at the collapse stage at the scale of the thickness of the forming structures. While relying on these theoretical predictions, Codis et al. (2012) speculated that secondary shell-crossing could lead to the formation of vortices aligned with the forming filament. In turn these vortices would account for the spin of these halos. There is now indeed ample numerical evidence that the evolution of galaxy morphology is likely to be in part driven by the geometry of the cosmic web, and in particular its vorticity content.

Hence our focus will be in revisiting these findings with an emphasis on *where* (tracing the filaments) and *why* (studying the origin of the vorticity and its orientation) these trends are detected. We will also tentatively explain the origin of the mass transition for halo-spin alignment with the LSS's filaments. This paper aims at revisiting early stages of AM acquisition corresponding to when the cold gas/DM is expelled from neighbouring voids and walls. The main question addressed in this work will be: are there statistical evidence that swirling filaments are responsible for spinning up dark halos and gaseous discs?

The focus will be specifically exclusively on lower mass halos ($M_{\odot} < 5\,10^{12}$) for which secondary anisotropic infall (originating from the vortex-rich filament within which they form) dominates their angular momentum budget. To that end, we will in particular make use of filament and wall tracers in order to quantify the cosmic web, which is the natural metric for galactic evolution. The virtual data used will be dark matter and hydrodynamical simulations.

This paper is organized as follows. Section 2 describes the simulations and the estimators implemented in this paper. Section 3 sums up robust statistical results of i) the orientation of the vorticity relative to the filaments, ii) the distribution of the vorticity inside the filament and iii) the alignment of the spin of dark halos with the vorticity. Section 4 explores qualitatively the origin of this vorticity and uses the link between vorticity and spin to explain the non-monotonic behaviour of spin-filament alignment for haloes with masses lower than $M_{\rm crit}$. Section 5 wraps up and discusses implications. Appendix A finds consistency in alignment with the vorticity of adiabatic/cooling gas. Appendix B studies the effect of scale on the alignment. Ap-

Name	**Type**	**Box size** h^{-1} Mpc	**Resolution**	$\mathbf{R}_{\rm velocity}$ h^{-1} Mpc	$\mathbf{R}_{\rm density}$ h^{-1} Mpc	$\mathbf{R}_{\rm Lagrangian}$ h^{-1} Mpc	**Minimum halo mass** $10^{10} M_\odot$
$\mathcal{S}_{100}^{\rm CDM}$	ΛCDM	100	256^3	0.39	2.3	–	44
$\mathcal{S}_{100}^{\rm HDM}$	ΛHDM	100	256^3	0.39	2.3	2.3	–
$\mathcal{S}_{50}^{\rm CDM}$	ΛCDM	50	$256^3 \times (20)$	0.78	1.2	–	6.2
$\mathcal{S}_{20}^{\rm CDM}$	ΛCDM	20	512^3	0.039	0.23	–	0.044
$\mathcal{S}_{20}^{\rm HDM}$	ΛHDM	20	512^3	0.039	0.23	0.23	–
$\mathcal{S}_{2000}^{\rm CDM}$	ΛCDM	2000	4096^3	–	5	–	77

Table 1. The set of simulations used in Sections 3 and 4. The so-called ΛHDM subset corresponds to simulations, the initial condition of which have been smoothed over 2.3 h^{-1} Mpc and 0.23 h^{-1} Mpc. The simulation $\mathcal{S}_{2000}^{\rm CDM}$ corresponds to the post-processing of an HPC simulation which allowed us to identify over 34 millions halos. The velocity field, density field, initial conditions were smoothed with Gaussian filter. In this work, we consider halos with more than 100 particles.

pendix C analyses the orientation of the vorticity w.r.t. the tidal field eigendirections.

2 DATASETS AND ESTIMATORS

All the statistical results of Section 3 rely on a set of dark matter standard ΛCDM simulations presented in table 1. These simulations are characterized by the following ΛCDM cosmology: $\Omega_{\rm m} = 0.24$, $\Omega_\Lambda = 0.76$, $n = 0.958$, $H_0 = 73\,{\rm km.s^{-1}\,Mpc^{-1}}$ and $\sigma_8 = 0.77$ within one standard deviation of WMAP3 results (Spergel et al. 2003).

We use different box sizes: a 100 h^{-1} Mpc box with an initial mean spatial resolution of 390 h^{-1} kpc (256^3 DM particles) in order to build a statistical sample of halos and filaments, several 50 h^{-1} Mpc boxes with a mean spatial resolution of 190 h^{-1} kpc (256^3 particles), and a 20 h^{-1} Mpc box with a mean spatial resolution of 39 h^{-1} kpc (512^3 particles). All these simulations were run with GADGET (Springel et al. 2001), using a softening length of $1/20^{\rm th}$ of the mean inter-particle distance. We also use the Horizon-4π simulation, a 2000 h^{-1} Mpc box $\mathcal{S}_{2000}^{\rm CDM}$ with 4096^3 DM particles (Teyssier et al. 2009).

In addition, the ΛHDM subset corresponds to simulations with initial conditions that have been smoothed with a Gaussian filtering on scales of 2.3 and 0.23h^{-1} Mpc respectively to suppress small scale modes for the purpose of visualization and interpretation. All simulations but the sets $\mathcal{S}_{50}^{\rm CDM}$, $\mathcal{S}_{2000}^{\rm CDM}$ share the same phases.

All the simulations are studied at redshift $z = 0$. The Friend-of-Friend Algorithm (or FOF, Huchra & Geller 1982) is used to define dark matter halos. In the present work, we only consider halos with more than 100 particles, which corresponds to a minimum halo mass of 44 $\times 10^{10}$ $M_\odot$ in $\mathcal{S}_{100}^{\rm CDM}$. For instance, 9028 halos were detected at redshift zero in $\mathcal{S}_{100}^{\rm CDM}$. The spin of a halo is defined as the sum over its particles i: $\sum_i (\mathbf{r}_i - \overline{\mathbf{r}}) \times (\mathbf{v}_i - \overline{\mathbf{v}})$ where $\overline{\mathbf{r}}$ is the center of mass of the FOF and $\overline{\mathbf{v}}$ its mean velocity. As discussed in Pueblas & Scoccimarro (2008), for the dark matter simulations we sample optimally the velocity field using a Delaunay tessellation. The vorticity of the velocity is then measured from the resampled velocity at each point of the 256^3 grid as the curl of the velocity field $\omega = \nabla \times \mathbf{v}$, after gaussian smoothing of the velocity field with a kernel length of 390 h^{-1} kpc for $\mathcal{S}_{100}^{\rm CDM}$ and $\mathcal{S}_{100}^{\rm HDM}$, a kernel length of 780 h^{-1} kpc for $\mathcal{S}_{50}^{\rm CDM}$ and a kernel length of 39 h^{-1} kpc for $\mathcal{S}_{20}^{\rm CDM}$ and $\mathcal{S}_{20}^{\rm HDM}$.

A comparison between vorticity maps in $\mathcal{S}_{20}^{\rm CDM}$ and in $\mathcal{S}_{20}^{\rm HDM}$ is shown in Fig. 1. Vorticity along the normal to the section is plotted in the right panels of this figure. In $\mathcal{S}_{20}^{\rm HDM}$, high frequencies features are suppressed but the low frequency vorticity remains consistent with that of the more realistic $\mathcal{S}_{20}^{\rm CDM}$. In $\mathcal{S}_{100}^{\rm HDM}$, the smoothing is chosen such that in high vorticity regions (defined here as being regions where the vorticity is greater than 20 per cent of the maximum vorticity), the mean vorticity is of the order of 90 $h\,{\rm km\,s^{-1}\,Mpc^{-1}}$, i.e it corresponds more or less to one revolution per Hubble time, in agreement with the theoretical predictions of Pichon & Bernardeau (1999). The orders of magnitude are similar in $\mathcal{S}_{100}^{\rm CDM}$, $\mathcal{S}_{20}^{\rm HDM}$ and $\mathcal{S}_{20}^{\rm CDM}$.

The cosmic network is identified with `rSeX` and `DisPerSE`, the filament tracing algorithms based either on watersheding (Sousbie et al. 2009), or persistence (Sousbie 2011; Sousbie et al. 2011) without significant difference for the purpose of this investigation. The first method identifies ridges as the boundaries of walls which are themselves the boundaries of voids. The second one identifies them as the "special" lines connecting topologically robust (filament-like) saddles points to peaks. In this paper, the scale at which the filaments are traced (6 pixels Gaussian for each simulation) corresponds to large enough scales so that we are investigating the flow relative to the LSS (though see Appendix B for variations). Filaments are defined as a set of small segments linking neighbours pixels together. The mean size of the segments is 0.6 pixels.

For comparison with previous studies (e.g. Libeskind et al. 2013), walls are defined according to the density Hessian. Given λ_i the eigenvalues of the Hessian $\mathcal{H} = \partial^2\rho/\partial {\rm r}_i \partial {\rm r}_j$ where ρ is the density field, with $\lambda_i > \lambda_j$ if $i < j$, walls are identified as being the region of space where $\lambda_1 > \lambda_2 > 0$ and $\lambda_3 < 0$. The normal of a wall is given by the direction of the eigenvector associated to λ_3. To obtain the Hessian, the density field of $\mathcal{S}_{100}^{\rm CDM}$ is smoothed with a Gaussian filter of 1.6 h^{-1}Mpc and differentiation of the density field is performed in Fourier space.

To estimate the number of multi-flow regions within the caustic and their size, for each segment of the skeleton, the vorticity cube is cut with a plane perpendicular to the direction of the filament. The number of multi-flow regions is given by the number of regions of positive and negative projected vorticity along this direction (with a given threshold), counted in a small window centred on the filament. To obtain the size of the regions with a given polarity, the area where the absolute projected vorticity along the normal is

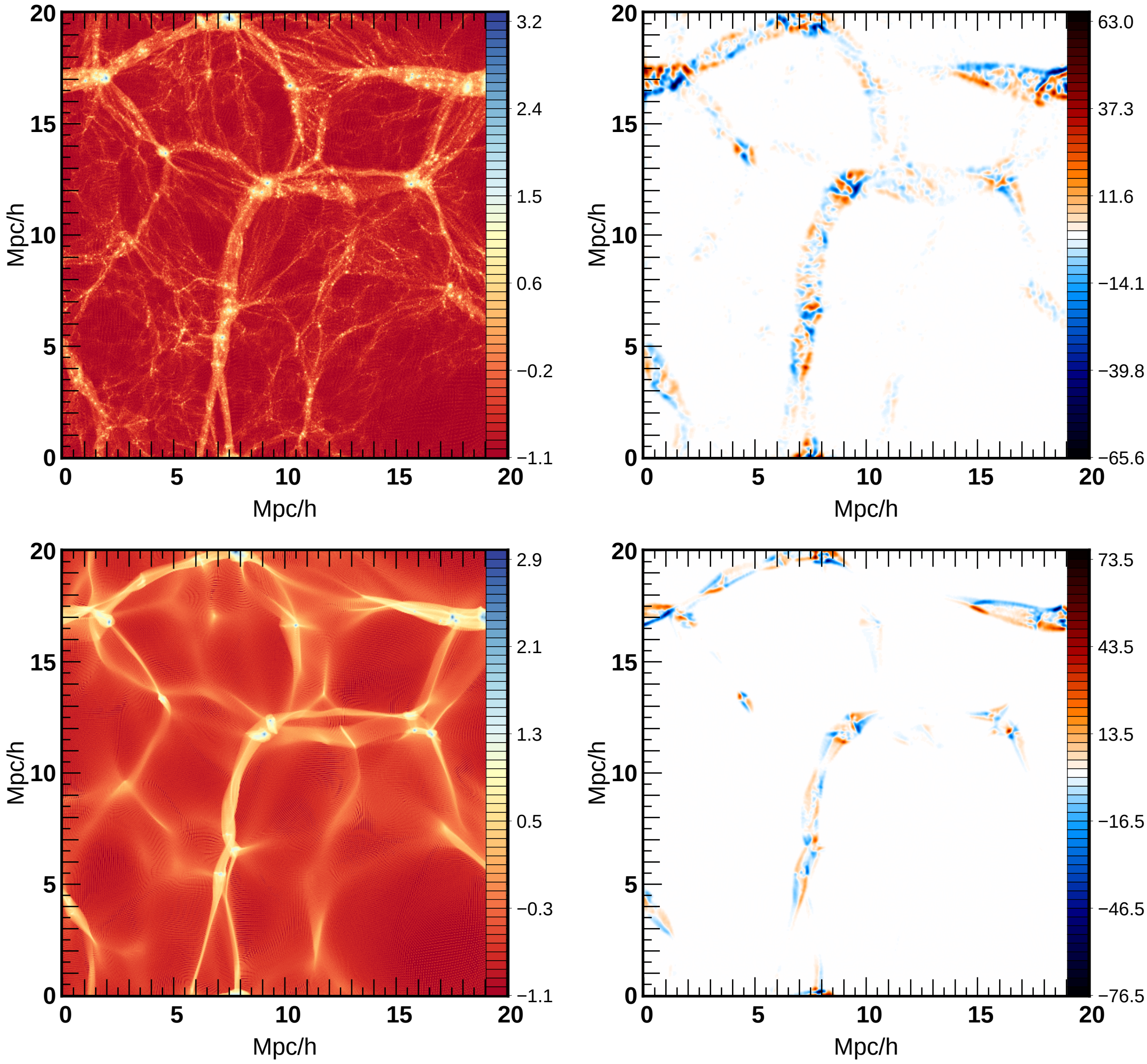

Figure 1. A thin slice ($2\,h^{-1}$ Mpc thickness) of the projected DM density (*left panels*) and the projected vorticity along the normal to the slice in unit of $h\,\mathrm{km\,s^{-1}\,Mpc^{-1}}$ (*right panels*). DM density is plotted with a logarithmic scale. Vorticity is computed after smoothing of the velocity field with a Gaussian filter of 160 h^{-1} kpc for this figure only. The geometry of the vorticity closely follow the LSS, but switches polarity across the walls/filaments (recalling that walls appear as filaments and filaments as peaks in such a cross section). Note also how the vorticity is localized around filaments (the 2D peaks, as exemplified on Fig. 7 below). The two panels allow for a comparison between a section of $\mathcal{S}_{20}^{\rm CDM}$ (*top*) and $\mathcal{S}_{20}^{\rm HDM}$ (*bottom*). In $\mathcal{S}_{20}^{\rm HDM}$, high-frequency modes are suppressed but the low-frequency vorticity is qualitatively consistent with that found in the realistic $\mathcal{S}_{20}^{\rm CDM}$. On the bottom left panel, the density caustics are quite visible and correspond to the outer edge of the multi-flow region in the bottom right panel.

greater than 10 per cent of the maximum vorticity is measured, and this area is divided by the number of quadrants. Assuming that these regions are quarter of disks, it yields the corresponding radius. This measure is done in $\mathcal{S}_{100}^{\rm HDM}$.

3 STATISTICAL ALIGNMENTS

Let us first present robust statistical results derived from sets of ΛCDM simulations.

3.1 Correlation between vorticity and filaments

The alignment of vorticity with the direction of the filaments is examined in $\mathcal{S}_{100}^{\rm CDM}$ and in $\mathcal{S}_{100}^{\rm HDM}$. The angle μ_1 between the direction of the vorticity and the direction of the filament is measured along each segment of the skeleton, and μ_2 between the direction of the vorticity and the direction of the normal of the wall. The probability distribution function (PDF) of the absolute value of the cosine of these angles is shown in Fig. 2. This PDF is normalized for $\cos\mu$ between 0 and 1. A strong detection is achieved. The signal is stronger in $\mathcal{S}_{100}^{\rm HDM}$ (because of a smoothing of high frequencies) but a clear signal is also detected in $\mathcal{S}_{100}^{\rm CDM}$. As a check, the alignment between vorticity and shuffled segment directions is then measured: no signal is detected.

In the filaments we find an excess of probability of 20 per cent to have $|\cos\mu_1|$ in $[0.5, 1]$ (that is $0 \leqslant \mu_1 \leqslant 60°$) relative to random orientations. In the walls, we find an excess of probability of 45 per cent to have $|\cos\mu_2|$ in $[0, 0.5]$

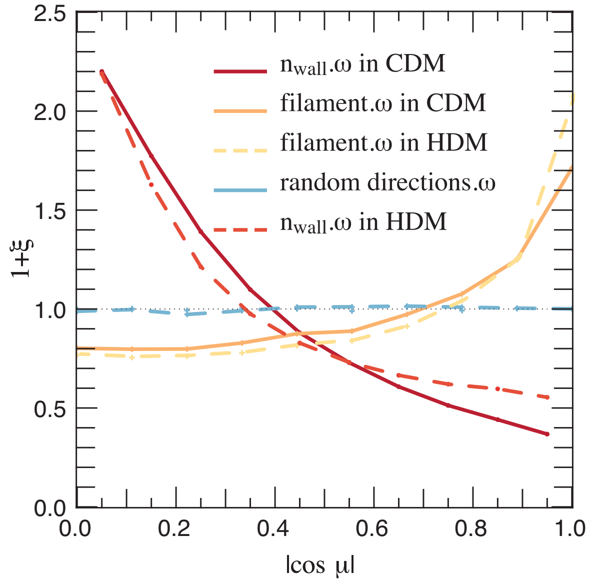

Figure 2. The probability distribution function of $\cos\mu$, the cosine of the angle between the vorticity and the direction of the filament (*orange*) and the angle between the vorticity and the normal of wall (*red*) measured in the simulations $\mathcal{S}_{100}^{\rm CDM}$ (solid) and $\mathcal{S}_{100}^{\rm HDM}$ (dashed). The black dotted line corresponds to zero excess probability for reference. The large-scale total vorticity is preferentially aligned with filament axis.

(that is $60^{\rm o} \leqslant \mu_2 \leqslant 90^{\rm o}$) relative to random orientations, which means a strong signal for the vorticity to be aligned with the filament, and perpendicular to the normal of the surrounding wall.

We conclude that in the neighbourhood of filaments, vorticity is preferentially aligned with the filament's axis and perpendicular to the normal of walls. In other words, vorticity tends to be perpendicular to the axis along which material is collapsing fastest. This result is consistent with Libeskind et al. (2013), which explored the correlation between vorticity and shear eigenvectors. This correlation is confirmed in Appendix C.

3.2 Geometry of the multi-flow region

Since section 3.1 showed that vorticity tends to be aligned with the filamentary features of the cosmic web, we are naturally led to focus on the structure of high vorticity regions. The kinematics of the cross sections of the filaments is therefore examined, by cutting our simulation with a plane perpendicular to the direction of the filament. We represent in this plane the projected vorticity along the filament. Results are shown in Fig. 3 and can be summarized as follows: (i) vorticity is null outside the multi-flow region, and so confined to filaments (and walls in a weaker way) which is consistent with the assumption that cosmic flows are irrotational before shell-crossing; (ii) the cross sections of the filaments are partitioned into typically quadripolar multi-flow regions (see Fig. 4) where the vorticity is symmetric with respect to the center of the (density) caustic such that the global vorticity within that caustic is null (as expected); the typical size of each quadrant is of the order of a smoothing scale (as shown in Fig. 4); (iii) high-vorticity resides in the low-density regions of filaments: vorticity is mainly located at the edge of the multi-flow region *on* the caustic (see also Fig. 10 below); vorticity is in fact typically null *at* the peak of density. (iv) Each quadrant of the multi-flow region is fed by multiple flows, originating from neighbouring walls (see Fig 9).

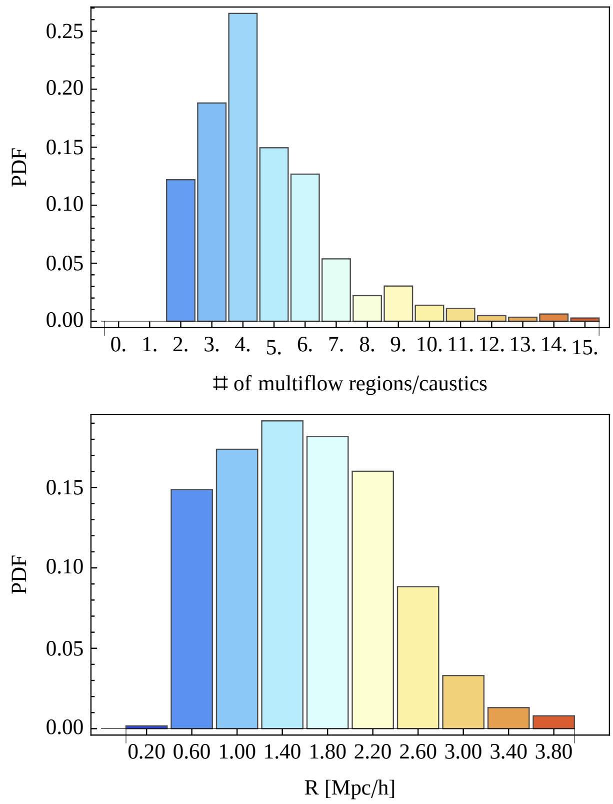

Figure 4. *Top:* Normalized histogram of the number of multi-flow regions with different polarity around a filament measured in the simulation $\mathcal{S}_{100}^{\rm HDM}$. The mean corresponds to $\langle n_{\rm multiflow}\rangle = 4.6$, the median is 4.25. On large scales, the multi-flow region is therefore typically quadrupolar. *Bottom:* Normalized histogram of the size of a region in $\mathcal{S}_{100}^{\rm HDM}$ with a given polarity. The mean size of such region is $\langle R\rangle = 1.6\,h^{-1}\,$Mpc, somewhat below the smoothing length of the initial conditions, $R_s = 2.3\,h^{-1}\,$Mpc. It was checked on $\mathcal{S}_{20}^{\rm HDM}$that a similar scaling applies.

3.3 Correlation between vorticity and spin

The alignment of vorticity with filaments on the one hand, and previous results about alignment (or orthogonality) of the low-mass (high-mass) halos spin with the filament and the shear eigenvectors (Codis et al. 2012; Libeskind et al. 2012) on the other hand, suggest to revisit the alignment of spin with the vorticity (previously examined by Libeskind et al. 2012) and to analyze in depth the correlation between vorticity and angular momentum. The measurement is done by computing the vorticity at the positions of the halos and the projection, $\cos\theta$, between both normalized vectors. First note that halos typically stand within one quadrant of the vorticity within filaments and not at the intersection of these quadrants, which is why the spin/vorticity alignment is strong.

The resulting PDF of $\cos\theta$ is displayed in Fig. 5. Here the set of simulations, $\mathcal{S}_{50}^{\rm CDM}$ are used to compute error bars

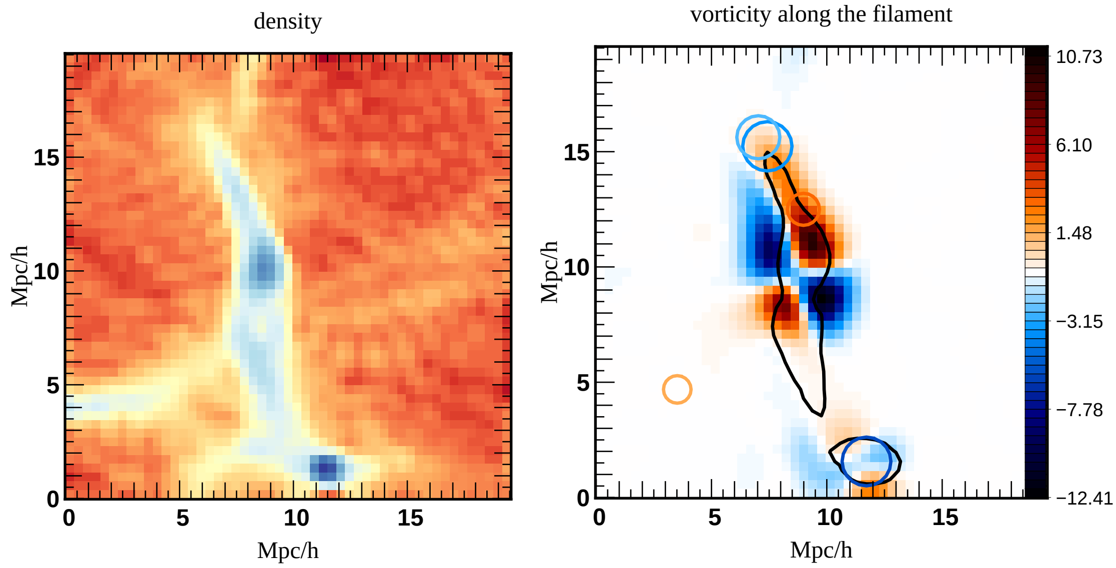

Figure 3. Geometry/kinematics of a typical multi-flow region across a filament. *Left:* density map of a section perpendicular to a given filament in logarithmic scale. *Middle*: projected vorticity along the filament within that section (towards observer in red and away from the observer in blue) in units of $h\,\mathrm{km\,s^{-1}\,Mpc^{-1}}$ on which is plotted in dark a contour of the density. Circles are halos with their corresponding virial radius. The colour of the circles match to the values of $\cos\theta$ between the halos spins and the normal of the section, positively oriented toward us. For this figure only, vorticity is computed after smoothing the velocity field with a Gaussian filter of 1.6 h^{-1} Mpc.

on the correlation between spin and vorticity. The measured correlations are noisier as only a finite number of dark halos are found within the simulation volume. It was checked that the correlation is not dominated by the intrinsic vorticity of the halos themselves by computing the alignment between the spin and the vorticity of the field *after extruding* the FOF halos, which led to no significant difference in the amplitude of the correlation. We find an excess probability of 25 per cent relative to random orientations to have $\cos\theta$ in $[0.5, 1]$ for halos with $10 \leqslant \log(\mathrm{M/M_\odot}) \leqslant 11$, 55 per cent for $11 \leqslant \log(\mathrm{M/M_\odot}) \leqslant 12$ and 165 per cent for $12 \leqslant \log(\mathrm{M/M_\odot}) \leqslant 13$. Note importantly that the intricate geometry of the multi-flow region (see also Fig. 7 and Fig. D1 below) strongly suggests retrospectively that the alignment (including polarity) between the spin of dark matter halos and the vorticity of the flow within that region cannot be coincidental.

Fig. 6 below, which presents PDF of the cosine of the angle between the spin of 43 million dark halos and the direction of the closest filament identified in the $\mathcal{S}^{\mathrm{CDM}}_{2000}$ simulation, displays an interesting feature at low mass. For the range of mass $\log M/\mathrm{M_\odot} \sim 11.5-12.5$, the actual alignment between the spin and the direction of the filament *increases* with mass, before it becomes abruptly perpendicular around $5\times10^{12}\,\mathrm{M_\odot}$. This is fully consistent with the corresponding increase in vorticity shown on Fig. 5, and will be discussed further in the next section.

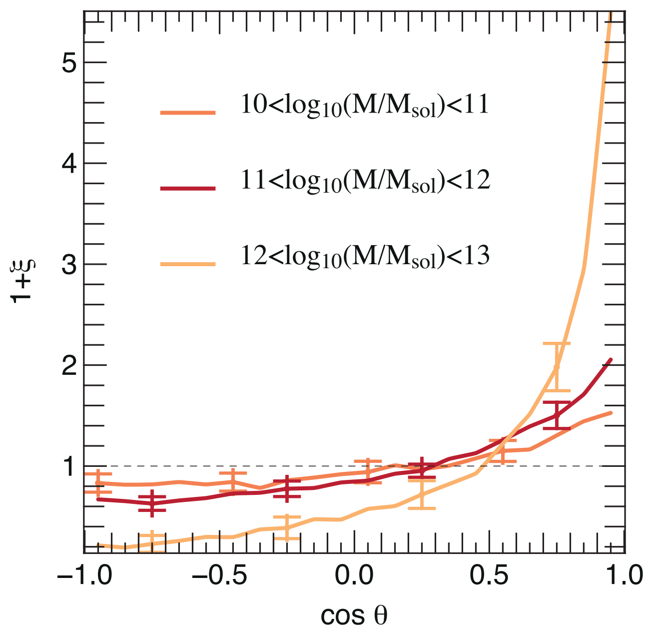

Figure 5. The probability distribution function of the angle between the vorticity and the spin measured in 20 simulations of the $\mathcal{S}^{\mathrm{CDM}}_{50}$ set. Halos are binned by mass as labeled. The displayed error bars are 1-σ standard deviation on the mean.

4 INTERPRETATION

Let us now turn to the visualization of special purpose simulations, the ΛHDM set, to identify the origin and implications of the measured vorticity of Section 3, and explain the observed mass transition.

4.1 Building up vorticity from LSS flow

Let us first show that density walls are preferentially aligned with zero-vorticity walls.

Fig. 7 displays the vorticity field in the neighbourhood of the main filament of the idealized "HDM" simulation, $\mathcal{S}_{20}^{\rm HDM}$. The vorticity bundle is clearly coherent on large scales, and aligned with the direction of the filament, strongest within its multi-flow core region, while its essentially quadrupolarity is twisted around it.

Fig. 8 displays the cross section of the vorticity perpendicular to the main filament shown in Fig. 7. The velocity field lines (in blue) converge towards the local walls (in brown) and are visually in agreement with the vorticity field which is partitioned by these walls. This picture is qualitatively consistent with the scenario presented in Codis et al. (2012), as it shows that the filaments are fed via the embedding walls, while the geometry of the flow generates vorticity within their core. This vorticity defines the local environment in which DM halos form with a spin aligned with that vorticity. The alignment between the contours of minimal vorticity and the density walls which is visually observed on Fig. 8 (left panel) is then quantitatively examined. The probability distribution of the cosine of the angle between the zero vorticity contour and the wall within the caustic is plotted on the right panel of Fig. 8 (see Appendix E for the definition of the zero vorticity contour). An excess of probability of 15 per cent is observed for $\cos\psi$ in $[0.5, 1]$ relative to random distribution, that is for the alignment of the walls with the minimal vorticity contours. This alignment increases with the smoothing of the tessellations, as expected.

4.2 Progenitors of multi-flow region

In a dark matter (Lagrangian) simulation, it is straightforward to identify the origin of particles within the multi-flow region. Fig. 9 traces back in time DM particles ending up within a quadrant of the multi-flow region. The quadrant is fed by three flows of particles. The flow is irrotational in the initial phase of structure formation until the crossing of three flows in the vicinity of the filaments generates shear and vorticity close to the caustic.

Note that the sharp rise near the edge of the multi-flow region at the caustic is qualitatively consistent with catastrophe theory (Arnold 1992), and is directly related to the prediction of Pichon & Bernardeau (1999). Fig. 10 illustrates this fact. To obtain this profile, a filament is cut in slices, corresponding to filament segments: each slice corresponds to a plane perpendicular to the direction of the segment. Local vorticity is measured within that plane and stacked. The amount of vorticity is greater near the caustic. These results are qualitatively consistent with the above-mentioned theoretical predictions which characterize the size and shape of the multi-flow regions after first shell crossing, and estimate their vorticity content as a function of cosmic time.

In short, having looked in detail at the set of (Lagrangian-) smoothed simulations allows us to conclude that streaming motion of dark matter *away* from minima and wall-saddle points of the field, and *along* the walls of the density field is responsible for generating the multi-flow region in which vorticity arises. In turn, this vorticity defines the environment in which lower mass halos collapse. Such halos inherit their spin from this environment, as quantified by Fig. 5.

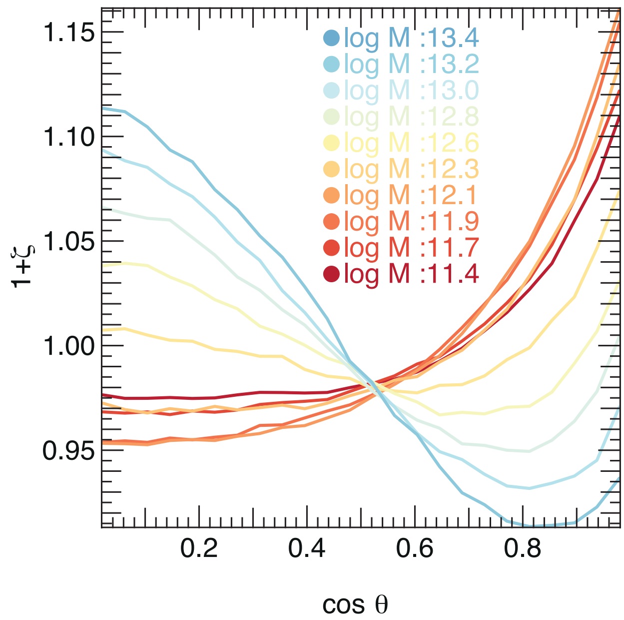

Figure 6. The probability distribution of the cosine of the angle between the spin of dark halos and the direction of the closest filament as a function of mass in the $\mathcal{S}_{2000}^{\rm CDM}$ simulation. The smoothing length over which filaments are defined is 5 h^{-1}Mpc. This figure extends the result first reported in Codis et al. (2012) to the mass range $\log {\rm M}/{\rm M}_\odot \sim 11.5$ - 12.0. In this mass range one observes that the probability to have a small angle between the halo's spin and the filament's direction first *increases* (in red) as mass grows to $\log {\rm M}/{\rm M}_\odot \sim 12.1$, in agreement with the increased spin - vorticity alignment demonstrated in Fig. 5. At larger masses (from orange to blue) the statistical spin-filament alignment quickly decays, with a critical mass (in yellow) corresponding to a transition to predominately orthogonal orientations (in blue) at $\log {\rm M}_{\rm crit}/{\rm M}_\odot \approx 12.7$ as defined by Codis et al. (2012).

4.3 Mass transition for spin-filament alignment

Up to now, we have not considered the mass of the forming halo within the multi-flow region. The assumption has been that the Lagrangian extension of the progenitor of the dark halo was small compared to the antecedents of a given vorticity quadrant, so that the collapse occurs within a quadrant of a given polarization, and leads to the formation of halos with a spin parallel to that vorticity. For more massive objets (of the order of the transition mass), we can anticipate that their progenitor patch overlap future vorticity quadrants of opposite polarity, hence that they will mostly cancel the component of their vorticity aligned with the filament as they form.The above-mentioned observed transition mass between aligned and anti-aligned spins relative to filaments would then typically correspond to the mass associated with the width of the quadrant of each caustics. In fact, as argued in Pichon & Bernardeau (1999, figure 7) and shown on Fig. 10, the vorticity within the multi-flow region is mostly distributed near the caustic, on the outer edge of the multi-flow region. It is therefore expected that, as the size of the collapsed halo increases, but remains *below* that of the quadrant, its vorticity should increase (as it collects more and more coherent rotating flow as secondary inflow), as shown on Fig. 5. As it reaches sizes *above* that of the quadrant, it should start to diminish significantly[1] (see also Fig. 11 below).

Let us turn back specifically to Fig. 6. For the range of mass $\log \mathrm{M}/\mathrm{M}_\odot \approx 11.4 - 12.1$, the alignment between the spin and the direction of the filament *increases* with mass, peaking at $\mathrm{M}_{\max} \approx 10^{12}\,\mathrm{M}_\odot$, before it rapidly decreases and changes to preferably perpendicular one for $\log \mathrm{M} > \log \mathrm{M}_{\mathrm{crit}} \approx 12.7$, i.e $\mathrm{M}_{\mathrm{crit}} \approx 5 \times 10^{12}\,\mathrm{M}_\odot$. This is fully consistent with the corresponding increase in vorticity shown on Fig. 5.

The characteristic masses can be roughly understood by conjecturing that the highest alignment occurs for the haloes which are of the size of vortices in the caustic regions that *just* undergo collapse. The measured caustic structure depends on the chosen smoothing scale, so a recently formed filament corresponds to the vortex that shows a basic four quadrant structure and, following Pichon & Bernardeau (1999) which has vorticity close to the Hubble value H. From our simulations, the typical Lagrangian radius of such vortex is $\approx 1.5\,h^{-1}\,\mathrm{Mpc}$ which if taken as the top-hat scale, gives a mass estimate $\mathrm{M}_{\max} \approx 1.5 \times 10^{12}\,\mathrm{M}_\odot$ for the mass of halos with maximum spin/filament alignment. The transition to misalignment will happen at $\mathrm{M}_{\mathrm{crit}} \approx 8 \times \mathrm{M}_{\max}$ where the whole width of the filament is encompassed. Of course the quantitative accuracy of such argument should not be over-emphasized. For instance, if we took the Lagrangian radius of the vortex to be $1.3\,h^{-1}\,\mathrm{Mpc}$, we would get $\mathrm{M}_{\max} = 10^{12}\,\mathrm{M}_\odot$, which would fit the transition of Fig. 6 even closer.

5 DISCUSSIONS & CONCLUSIONS

Let us reframe the findings of Section 3 and 4 in the context of recent published results in this field, before concluding.

5.1 Discussion

Libeskind et al. (2013)'s description of AM acquisition occurs in two stages (first through TTT, then through the curl of the embedding velocity field). Results of section 3 and 4 seem consistent with this. In particular the alignment of vorticity with the eigen vectors of the tidal field is confirmed in Appendix B. The connection between Pichon et al. (2011) and this paper is the following: in the former, it was shown that the spin up of dark halos proceeded in stages: a given collapsing halo would first acquire some specific angular momentum following TTT, at turn around freezing its amplitude at the TTT expected value; in a secondary stage (see their Fig. 9), it would spin up again as it acquires specific angular momentum from secondary infall coming from the larger scale distribution of matter which collapses at the next stage of hierarchical clustering. For relatively isolated massive halos that form from statistically rare density enhancements as studied in Pichon et al. (2011), this secondary collapse just leads to a virialized halo of increased mass. The emphasis of the current paper and of Codis et al. (2012) (see also Danovich et al. 2011) is to note that for less massive and less rare halos, forming in large-scale filamentary regions, this secondary infall, coming late from the turn-around of the encompassing filamentary structure, is arriving along marked preferred directions and is typically multi-flow and vorticity rich. Given that the shell crossing occurring during the later formation of that embedding filament generates vorticity predominantly aligned with the filament, this secondary infall will contribute extra spin-up along the filament direction. Hence the global geometry of the inflow is consistent with a spin acquisition for halos induced by the large-scale dynamics within the cosmic web, and in particular its multi flow vortices. This scenario may only be reconciled with the standard tidal torque theory if the latter is augmented so as to account for the larger scale anisotropic environment of walls and filaments responsible for secondary infall.

One could anticipate that taking into account the anisotropy of the longwave modes that form the environment of the proto-halo in the spirit of peak-background split formalism (Kaiser 1984, PBS) should allow us to explain the alignment of the halos' spin within filaments. Indeed, it can be shown that the tidal field near a wall and a filament would impact the possible mis-alignment of the shear tensor and the inertia tensor of a collapsing peak. On the basis of what was found in this paper, the following extra caveats to the extension of PBS should nonetheless also be added for low mass dark halos (below the transition mass): i) the dark matter particles originating from its original Lagrangian patches reach the filament from multiple directions; ii) the flow from the first two Lagrangian patches (see Fig. 9) reaching the same Eulerian patch within that filament may tidally spin-up the proto-halo (embedded in the third patch) in a manner which is not natively taken into account by TTT. In short, single shell TTT describes well the process of angular momentum acquisition for a halo up to the point when non-linearities on scales larger than that of the halo grow and turn around, as they may spin up additionally the halo. Depending on the rareness of the collapsing object, the two stages (primary versus secondary infall) may or may not be distinct and overlap in time.

For rarer halos this was interpreted as the conversion of the orbital momentum of satellites into spin, as the larger volume virializes. When the corresponding large-scale environment is filamentary, less rare halos will also be torqued by multiple infalling streams (which may not reach virialization), acquiring a spin aligned with the vortices of the large-scale flow. Indeed, this secondary infall brings-in the vorticity generated during the larger scale multi-flow collapse of that envelope[2]. Of course, usual TTT could still be applied to an extended region around a lower mass halo which encompasses its inner plus outer patch, and predict

[1] In fact, while investigating the statistics of the vorticity within spherical shells, Pichon & Bernardeau (1999) showed that if we consider spheres of size above one quadrant of the multi-flow regions, the total vorticity within that sphere drops significantly.

[2] or quite equivalently, the green and blue flows in Fig. 11 will tidally spin up the halo as it enters the multi-flow region.

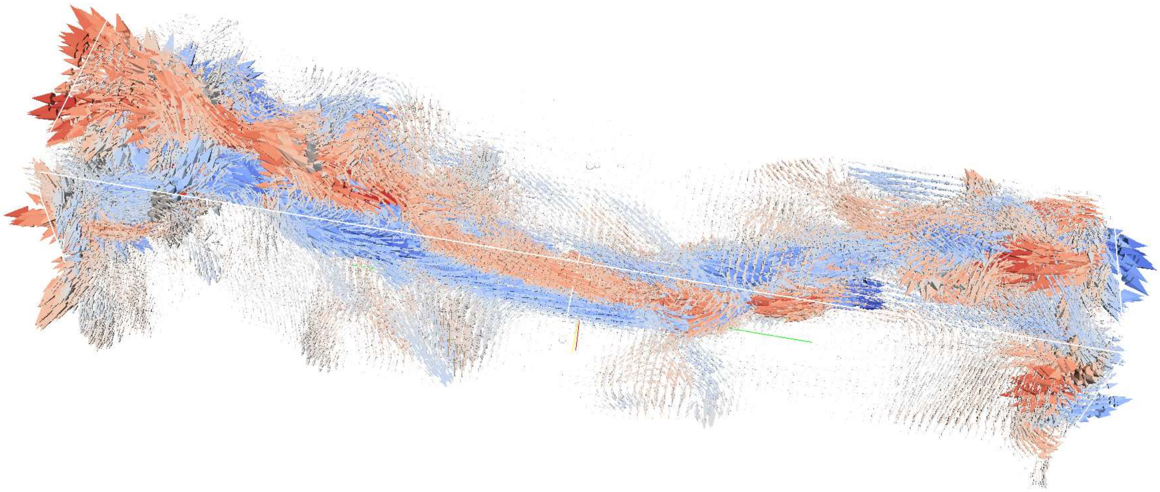

Figure 7. Vorticity field in the neighbourhood of the main filament of the idealized "HDM" simulation, $\mathcal{S}_{20}^{\rm HDM}$ colour coded through its 'z' component. The vorticity is clearly aligned with the direction of the filament, strongest within its multi-flow core region, while its polarity is twisted around it. Helicity measurements are consistent with the observed level of twisting.

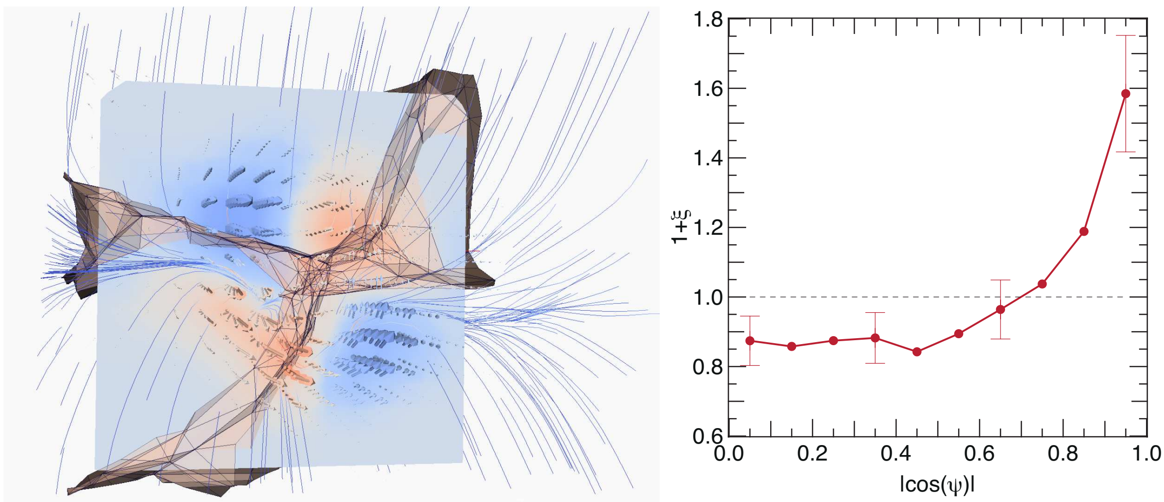

Figure 8. *Left:* the cross section of the vorticity perpendicular to the main filament shown in Fig. 7. The colour coding in the section corresponds to the vorticity towards us (in blue) and away from us (in red) as shown by the corresponding arrows. The thin blue lines correspond to velocity field lines. The brown surfaces represent the local walls. The field lines converge towards the local walls and are in agreement with the vorticity field which is partitioned by these walls. *Right:* the probability distribution as a function of the cosine angle between the normal to the zero vorticity walls and the normal to the density walls, $\cos\psi$, computed on the simulation $\mathcal{S}_{100}^{\rm CDM}$. The simulation is divided into eight 50 h^{-1} Mpc sub-boxes. Density walls are computed using `DisPerSE`, and the smoothing coefficient of the tessellation is S=4 (see Appendix E). The plotted signal corresponds to the average of the PDFs for the 8 sub-boxes. The displayed error bars are 1-σ standard deviation on the mean.

correctly the mean angular momentum within that *region* but it does not resolve the individual spin of the embedded low-mass halo.

Yet, it should be possible to reconcile this process with TTT through a non-local two-stages extension of it, where the significant drift of dark matter (corresponding to what will be part of the halo after PBS collapse) towards its filament, and within its wall, is taken into account. Let us sketch the basis of such calculation. The geometry of the setting is shown on Fig. 11. For Gaussian random fields, one should be able to compute the most likely tidal field and inertia tensor at a given Lagrangian peak, subject to a Zel'dovich boost which will translate that peak near to a filament at some distance **r**; this distance corresponds to the time during which the nearby filament has shell-crossed multiplied by the original velocity. In turn, the condition of shell crossing can be expressed as constraints on the eigenvalues of the shear tensor. As argued above, we can anticipate that the pre-existing Lagrangian correlation between the tidal field of the halo-to-be on the one hand, and the Hessian of the filament-to-be on the other hand, will impose some alignment between the direction of the filament (along the first eigenvector of the Hessian) and the spin of the collapsing halo (as set by the corresponding tidal tensor). If the condition that the fila-

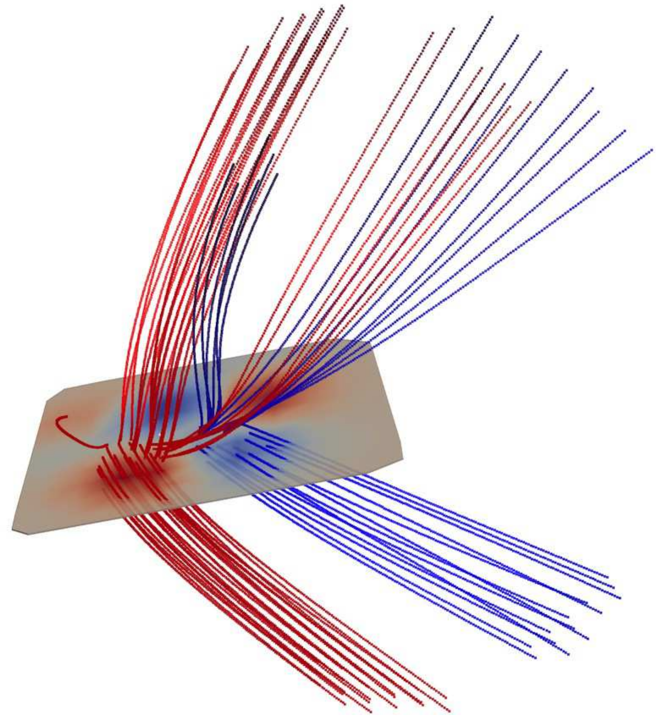

Figure 9. *Left*: Individual dark matter particles trajectories ending in a given quadrant of the vorticity multi-flow region. In blue are particles ending in a region of positive projected vorticity along the filament, and in red the particles ending in the negative vorticity region. The quadrant is fed by at least three flows of particles (See also the inset in Fig. 11, which represents qualitatively the theoretical expectation of the starting points of these bundles in the Zel'dovich approximation). The $\mathcal{S}^{\rm HDM}_{100}$ simulation is used for this figure.

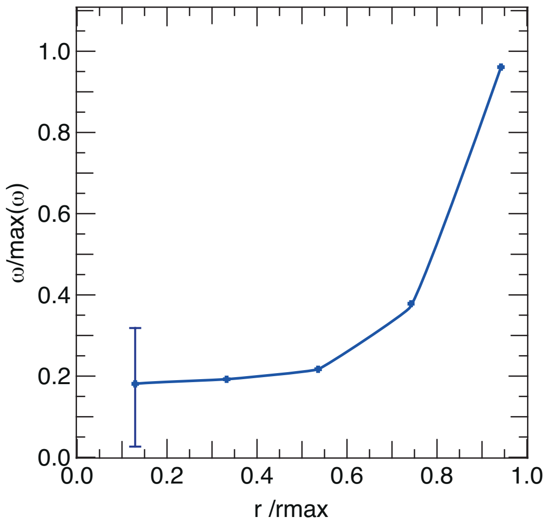

Figure 10. Azimuthal average of the radial profile of the vorticity. The profile is obtained by averaging on the sections of a complete filament (each section is associated to a filament segment, to which the section is perpendicular). Vorticity is clearly larger towards the caustic, and would theoretically become singular (as $1/\sqrt{1-r/r_{\rm max}}$) *at* the caustic for a Zel'dovich mapping, as shown in Pichon & Bernardeau (1999). Here the profile is convolved by shape variations from one caustic to another and by the azimuthal average. The indicative error bar was computed as the average over a larger stack.

Definition	**Name**	**Mean**	**Median**
Alignment between vorticity and Cosmic Web			
DM: vorticity/filaments		0.58 (0.5)	0.62
Hydro: vorticity/filaments	$\lvert\cos\mu\rvert$	0.58 (0.5)	0.63
DM: vorticity/walls		0.34 (0.5)	0.27
Alignment between vorticity and halos spin			
$10 \leqslant \log(M/{\rm M}_{\odot}) \leqslant 11$		0.09 (0.0)	0.14
$10 \leqslant \log(M/{\rm M}_{\odot}) \leqslant 12$	$\cos\theta$	0.19 (0.0)	0.29
$12 \leqslant \log(M/{\rm M}_{\odot}) \leqslant 13$		0.53 (0.0)	0.72
Alignment between density walls and 0-vorticity walls			
	$\lvert\cos\psi\rvert$	0.54 (0.5)	0.56
Alignment between vorticity and tidal tensor eigenvectors			
vorticity / e1		0.62 (0.5)	0.69
vorticity / e2	$\lvert\cos\gamma\rvert$	0.48 (0.5)	0.47
vorticity / e3		0.31 (0.5)	0.23

Table 2. The median and mean cosine values for the set of studied alignments. In parenthesis, the expected values for random distributions.

ment is embedded into a given wall is added, the axial symmetry of the problem will be broken, and the inertia and tidal tensor (which are sensitive to different scales) will end up misaligned, reflecting this anisotropy. In this context, the observed spin (and importantly its polarity) would correlate with the polarity of the vorticity quadrant the halo ends up into after translation. The upshot is that on Fig. 11, the lighter pink sphere would "know" about the green dots given these constraints. This supplementary requirement is imposed by the fact that the correlation between spin and vorticity keeps tract of the direction of both vectors, as shown on Fig. 5. Though this computation will not be completely trivial, similar kind of two-point conditional correlations for the spin of collapsing structures have recently been carried out by Giahi & Schäfer (2013). Note that, as discussed previously, it is clear from this sketch that, as the Lagrangian patch of the proto-halo becomes of the order of the typical Lagrangian size of the quadrant, the alignment will increase, and as it becomes larger, it will fade. Note finally that this "one slice perpendicular to the filament axis" picture cannot address the process of spin flipping to a perpendicular direction to the filament via mergers, as this is a longitudinal, non-linear process (Peirani et al. 2004). This will be the topic of further work in this context.

5.2 Conclusions

Using large-scale cosmological simulations of structure formation, we have analyzed the kinematic properties of the velocity flows relative to the cosmic web. Our findings are the following:

- The vorticity in large-scale structures on scales of 0.39 h^{-1} Mpc and above is confined to, and aligned with its filaments with an excess of probability of 20 per cent relative to random orientations, and perpendicular to the normal of the dominant walls at a similar level. This is consistent with the corresponding direction of the eigenvectors of the tidal field (and is expected given that the potential is a smoothed version of the density field).

- At these scales, the cross sections of these filaments are typically partitioned into quadripolar caustics, with opposite vorticity parallel to their filament, arising from multiple flows originating from neighbouring walls, as would secondary shell crossing along these walls imply. The radial vorticity profile within the multi-flow region displays a sharp rise near the caustic, a qualitatively expected feature of catastrophe theory.
- The spins of embedded halos within these filaments are consistently aligned with the vorticity of their host vorticity quadrant at a level of 165 per cent. The progenitor of lighter halos within the multi-flow region can be traced back to three flows or more originating from the neighbouring walls, and form within the filament.
- Appendix A shows that for adiabatic/cooling hydrodynamical simulations within the dark matter caustics, the gas and the dark matter share the same vorticity orientation on large scales. High-resolution cooling runs show that the small scale structure of the velocity flow around forming galaxies does not destroy this larger scale coherence.
- The mass transition for spin-filament alignment is set by the size of sub-caustics with a given polarization. The alignment is strongest for Lagrangian patch commensurable with the sub-caustic as vorticity is strongest on the edge of the multi-flow region. Once the collapsed halo has a size larger than any such sub-caustic, it cancels out most of the vorticity within the caustics.

The focus of this paper was in explaining the "where": pinning down the locus of vorticity and describing the geometry of multi-flow infall towards filaments; and the "how": explaining its origin via shell crossing. It also provided an explanation for the origin of the mass transition for spin alignment. All measured alignments are summarized in Table 2.

Improvements beyond the scope of this paper include i) developing the sketched anisotropic (filamentary) peak-background-split theory of spin acquisition; ii) quantifying the curvilinear evolution of the vorticity (orientation and amplitude) as a function of distance to the critical points of the cosmic web and predicting the spin flip for high masses; iii) quantifying the helicoidal nature of gas infall on galactic scales; iv) connecting the findings of this paper to the actual process of *galactic* alignment.

In turn, this should allow astronomers to shed light on the following problems: how and when was the present Hubble sequence of galaxies established? How much of the dynamical evolution of galaxies is driven by environment? What physical processes transforming galaxies dominates morphology: galaxy interactions and mergers, external accretion and outflows, secular evolution? What is their respective roles in shaping disks, bulges or spheroids? Is it the same process at low and high redshift? These are addressed in part in the companion paper, Welker (2014), which shows in particular using state-of-the-art hydrodynamical simulations with AGN/SN feedback, that at high redshifts, the large vorticity of the gas flow is correlated with the direction of the spin of *galaxies*.

Acknowledgments

We thank M. Haehnelt, James Binney and D. Lynden-Bell for useful comments during the course of this work. JD and AS's research is supported by Adrian Beecroft, the Oxford Martin School and STFC. Let us thank D. Munro for freely distributing his YORICK programming language and OPENGL interface (available at `http://yorick.sourceforge.net`). Some visualizations made use of the software PARAVIEW `http://www.paraview.org`. This research is part of the Horizon-UK project and Spin(E) supported by the grant ANR-13-BS05-0002 of the French *Agence Nationale de la Recherche*. CP thanks the PEPS "Physique théorique et ses interfaces" for funding, the institute of Astronomy for a Sacker visiting fellowship and the KITP for hospitality via the National Science Foundation under Grant No. NSF PHY11-25915.

References

Aragón-Calvo M. A., 2013, ArXiv e-prints
Aragón-Calvo M. A., van de Weygaert R., Jones B. J. T., van der Hulst J. M., 2007, *ApJ*, 655
Arnold V. I., 1992, Catastrophe theory / V.I. Arnold ; translated from the Russian by G.S. Wassermann ; based on a translation by R.K. Thomas, 3rd rev. and expanded ed. edn. Springer-Verlag Berlin ; New York
Aubert D., Pichon C., Colombi S., 2004, *MNRAS*, 352, 376
Bailin J., Steinmetz M., 2005, *ApJ*, 627
Birnboim Y., Dekel A., 2003, *MNRAS*, 345, 349
Codis S., Pichon C., Devriendt J., Slyz A., Pogosyan D., Dubois Y., Sousbie T., 2012, *MNRAS*, 427, 3320
Danovich M., Dekel A., Hahn O., Teyssier R., 2011, ArXiv e-prints
Doroshkevich A. G., 1970, Astrofizika, 6, 581
Dubois Y., Pichon C., Haehnelt M., Kimm T., Slyz A., Devriendt J., Pogosyan D., 2012, *MNRAS*, 423, 3616
Giahi A., Schäfer B. M., 2013, *MNRAS*, 428, 1312
Haardt F., Madau P., 1996, *ApJ*, 461, 20
Hahn O., Carollo C. M., Porciani C., Dekel A., 2007, *MNRAS*, 381, 41
Hoyle F., 1949, Problems of Cosmical Aerodynamics, Central Air Documents, Office, Dayton, OH. Central Air Documents Office, Dayton, OH
Huchra J. P., Geller M. J., 1982, *ApJ*, 257, 423
Kaiser N., 1984, *ApJ Let.*, 284, L9
Katz N., Keres D., Dave R., Weinberg D. H., 2003, in J. L. Rosenberg & M. E. Putman ed., The IGM/Galaxy Connection. The Distribution of Baryons at z=0 Vol. 281 of Astrophysics and Space Science Library, How Do Galaxies Get Their Gas?. pp 185–+
Kereš D., Katz N., Weinberg D. H., Davé R., 2005, *MNRAS*, 363, 2
Kimm T., Devriendt J., Slyz A., Pichon C., Kassin S. A., Dubois Y., 2011, ArXiv e-prints
Libeskind N. I., Hoffman Y., Forero-Romero J., Gottlöber S., Knebe A., Steinmetz M., Klypin A., 2013, *MNRAS*, 428, 2489

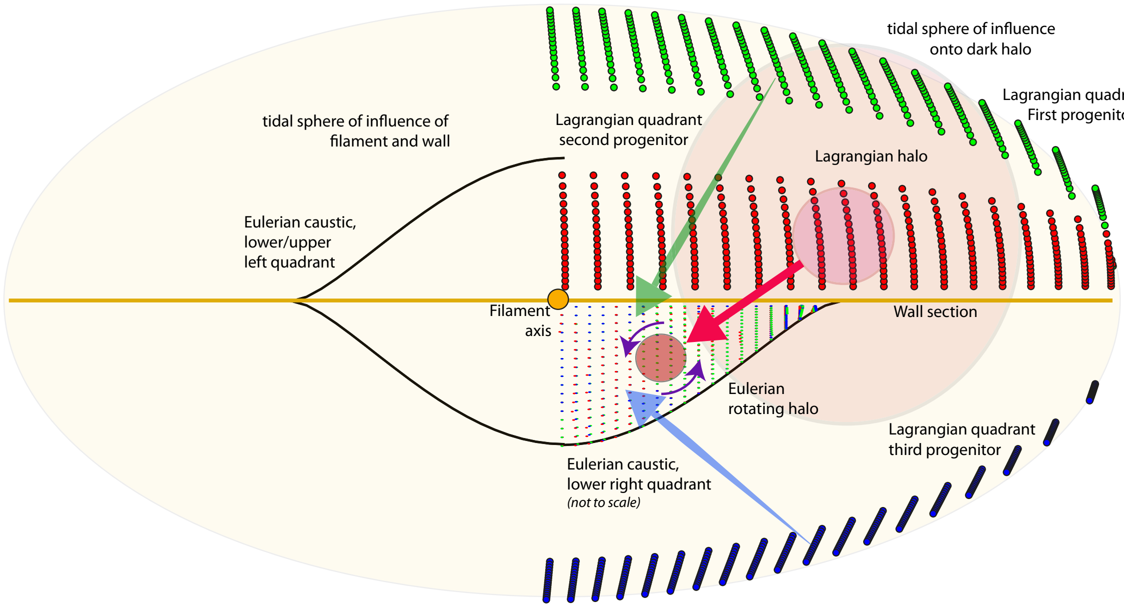

Figure 11. Sketch of the dynamics of a low mass halo formation and spin-up within a wall near a filament, which are perpendicular to the plane of the image (*in yellow*). The tidal sphere of influence of this structure is represented by the pale yellow ellipse. The three bundles of large dots (*in green, red, and blue*) represent Lagrangian points (at high redshift) which image, after shell crossing, will end up sampling regularly the lower right quadrant of the Eulerian multi-flow region; the three progenitor bundles are computed here in the Zel'dovich approximation (see Pichon & Bernardeau 1999, for details; note that this Eulerian quadrant is not up to scale). Each pair of dots (one large, one small) represents the same dark matter particle in the initial condition and final condition. In black, 3/4 of the Eulerian caustic. In light, resp. dark *pink*, the locus of the Lagrangian and Eulerian position of the halo, which has moved by an amount displayed by the *red* arrow, and spun up following the purple arrows while entering the quadrant. The *blue* and *green* arrows represent the path of fly-by dark matter particles originating from the other two bundles, which will contribute to torquing up the halo (following Codis et al. 2012). Given the geometry of the flow imposed by the wall and swirling filament, the spin of the dark matter halo will necessarily be parallel to the direction of the filament *and* to the vorticity in that quadrant. In the language of TTT, the tidal field imposed onto the Lagrangian patch of the halo (*very light pink*, corresponding to secondary infall) should be evaluated subject to the constraint that the halo will *move* into the *anisotropic multi-flow* region (each emphasis imposing a constraint of it own); these constraints will in turn impose that the corresponding spin-up will be aligned with the vortex.

Libeskind N. I., Hoffman Y., Knebe A., Steinmetz M., Gottlöber S., Metuki O., Yepes G., 2012, *MNRAS*, 421, L137

Libeskind N. I., Hoffman Y., Steinmetz M., Gottlöber S., Knebe A., Hess S., 2013, *ApJ Let.*, 766, L15

Ocvirk P., Pichon C., Teyssier R., 2008, *MNRAS*, 390, 1326

Paz D. J., Stasyszyn F., Padilla N. D., 2008, *MNRAS*, 389, 1127P

Peebles P. J. E., 1969, *ApJ*, 155, 393

Peirani S., Mohayaee R., de Freitas Pacheco J. A., 2004, *MNRAS*, 348, 921

Pichon C., Bernardeau F., 1999, *A&A*, 343, 663

Pichon C., Pogosyan D., Kimm T., Slyz A., Devriendt J., Dubois Y., 2011, *MNRAS*, pp 1739–+

Press W. H., Schechter P., 1974, *ApJ*, 187, 425

Prieto J., Jimenez R., Haiman Z., 2013, ArXiv e-prints

Pueblas S., Scoccimarro R., 2008, arXiv.org

Schaefer B. M., 2009, International Journal of Modern Physics D, 18, 173

Sousbie T., 2011, *MNRAS*, 414, 350

Sousbie T., Colombi S., Pichon C., 2009, *MNRAS*, 393, 457

Sousbie T., Pichon C., Kawahara H., 2011, *MNRAS*, 414, 384

Spergel D. N., Verde L., Peiris H. V., Komatsu E., Nolta M. R., Bennett C. L., Halpern M., Hinshaw G., Jarosik N., Kogut A., Limon M., Meyer S. S., Page L., Tucker G. S., Weiland J. L., Wollack E., Wright E. L., 2003, *ApJ Sup.*, 148, 175

Springel V., Yoshida N., White S. D. M., 2001, New Astronomy, 6, 79

Stewart K. R., Brooks A. M., Bullock J. S., Maller A. H., Diemand J., Wadsley J., Moustakas L. A., 2013, *ApJ*, 769, 74

Sutherland R. S., Dopita M. A., 1993, *ApJ Sup.*, 88, 253

Tempel E., Stoica R. S., Saar E., 2013, Monthly Notices of the Royal Astronomical Society, 428, 1827

Teyssier R., 2002, *A&A*, 385, 337

Teyssier R., Pires S., Prunet S., Aubert D., Pichon C., Amara A., Benabed K., Colombi S., Refregier A., Starck J.-L., 2009, *A&A*, 497, 335

Tillson H., Devriendt J., Slyz A., Miller L., Pichon C., 2012, ArXiv e-prints

Wang X., Szalay A., Aragón-Calvo M. A., Neyrinck M. C., Eyink G. L., 2013, ArXiv e-prints

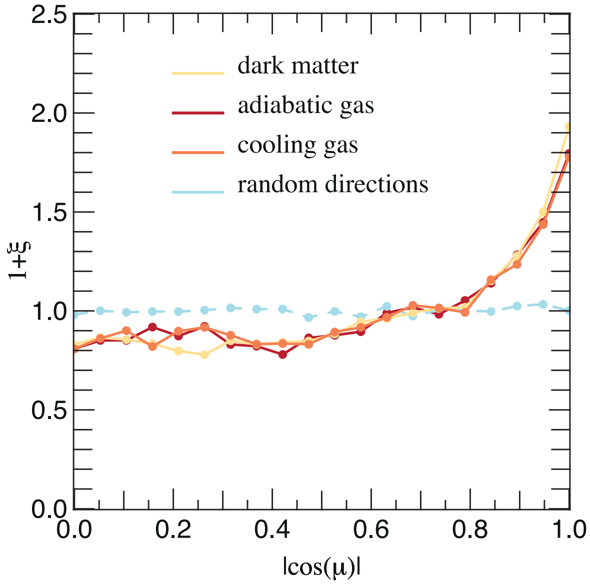

Figure A1. The probability distribution of the cosine of the angle between the vorticity in the smoothed DM and hydrodynamical simulations and the direction of the filament (solid line). The same measure is done for random directions of u (dashed blue line), plotted for the Dark Matter in $\mathcal{S}^{\rm HDM}_{100}$ and for the gas in $\mathcal{S}^{\rm HA}_{100}$ (adiabatic gas) and $\mathcal{S}^{\rm HC}_{100}$ (cooling run). We find an excess of probability for $|\cos\mu|$ in $[0.5, 1]$ relative to random orientations, and three profiles are very similar, which shows that large-scale modes dominate.

Name	Type	Box size h^{-1} Mpc	Resolution
$\mathcal{S}^{\rm HA}_{100}$	ΛHDM adiabatic	100	256^3
$\mathcal{S}^{\rm HC}_{100}$	ΛHDM cool	100	256^3
$\mathcal{S}^{\rm cool}_{20}(0.7)$	ΛCDM cool	20	1024^3

Table A1. The set of hydrodynamical simulations used in Appendix A. The hydro runs come in two categories: adiabatic and cooling, including one high resolution run which was stopped at redshift 0.7.

Welker C., 2014, submitted, 000

White S. D. M., 1984, *ApJ*, 286, 38

Zhang Y., Yang X., Faltenbacher A., Springel V., Lin W., Wang H., 2009, *ApJ*, 706, 747

Zhang Y., Yang X., Wang H., Wang L., Mo H. J., van den Bosch F. C., 2013, ArXiv e-prints

APPENDIX A: THE VORTICITY DISTRIBUTION OF THE GAS

We use three hydrodynamical simulations $\mathcal{S}^{\rm HA}_{100}$, $\mathcal{S}^{\rm HC}_{100}$ and $\mathcal{S}^{\rm cool}_{20}(0.7)$ (see also table A1), carried out with the Eulerian hydrodynamic code RAMSES (Teyssier 2002), which uses an Adaptative Mesh Refinement (AMR) technique. For these hydrodynamical runs, the evolution of the gas is followed using a second-order unsplit Godunov scheme for the Euler equations. The HLLC Riemann solver with a first-order Min-Mod Total Variation Diminishing scheme to reconstruct the interpolated variables from their cell-centered values is used to compute fluxes at cell interfaces. Collisionless particles (DM and star particles) are evolved using a particle-mesh solver with a Cloud-In-Cell interpolation. The initial mesh is refined up to $\Delta x = 1.7$ kpc according to a quasi-Lagragian criterion: if the number of DM particles in a cell is more than 8, or if the total baryonic mass in a cell is 8 times the initial dark matter mass resolution.

For the cooling runs $\mathcal{S}^{\rm cool}_{100}$, and $\mathcal{S}^{\rm cool}_{20}$, gas is allowed to cool by H and He cooling with an eventual contribution from metals using a Sutherland & Dopita (1993) model down to 10^4 K. Heating from a uniform UV background takes place after redshift $z_{\rm reion} = 10$ following Haardt & Madau (1996).

On large scales (as probed by the smoothed sets of simulations) the vorticity of gas shows the same correlations with the filaments as DM does. Fig. A1 displays the probability distribution of the cosine of the angle between the vorticity and the direction of the filament for the DM field (in red), the adiabatic gas (in blue) cooling run (in yellow). These three simulations quantitatively show the same preference for their vorticity to be aligned with the filamentary structure. In a nutshell, differences between the adiabatic and the cooling run only appear on kpc scales, so that on large scales, the dark matter, adiabatic and cooling runs have the same velocity field structure.

Fig. B1 displays the probability distribution of the cosine of the angle between the vorticity and the direction of the skeleton for a range of redshifts. The correlation between the direction of the filament and the vorticity is significant. As expected, this correlation decreases with cosmic time (at fixed smoothing scale). Appendix B investigates the evolution of this correlation as a function of the skeleton's persistence. As long as we consider large enough scales, the alignment pervades and is consistent with that of the dark matter. On smaller scales, the gas is dense enough to allow cooling to operate and re-structure the velocity flow. Notwithstanding, these smaller scale structures do not affect the larger scale correlation between vorticity and the direction of the filaments.

APPENDIX B: THE EFFECT OF PERSISTENCE ON ALIGNMENT

Given the characteristics of ΛCDM hierarchical clustering, one can anticipate that the process described in the main text occurs on several nested scales at various epochs - and arguably on various scales at the same epoch. The scenario we propose for the origin of vorticity and spin alignment is, like the signal itself, relative to the linear scale involved in defining the filaments and as such, multi-scale. Indeed in the main text, the two sets of simulations, $\mathcal{S}^{\Lambda\rm CDM}$ and $\mathcal{S}^{\Lambda\rm HDM}$, allowed us to probe different scales of the vorticity field. The induced multi-scale anisotropic flow also transpires in the scaling of the spin flipping transition mass with smoothing presented in Appendix D of Codis et al. (2012). It will hold as long as filaments are well defined in order to drive the local cosmic flow.

Let us now briefly explore the effects of probing different scales of the LSS via the skeleton level of persistence. Fig. B1 shows the excess alignment probability as a function of the cosine of the angle between the vorticity and the

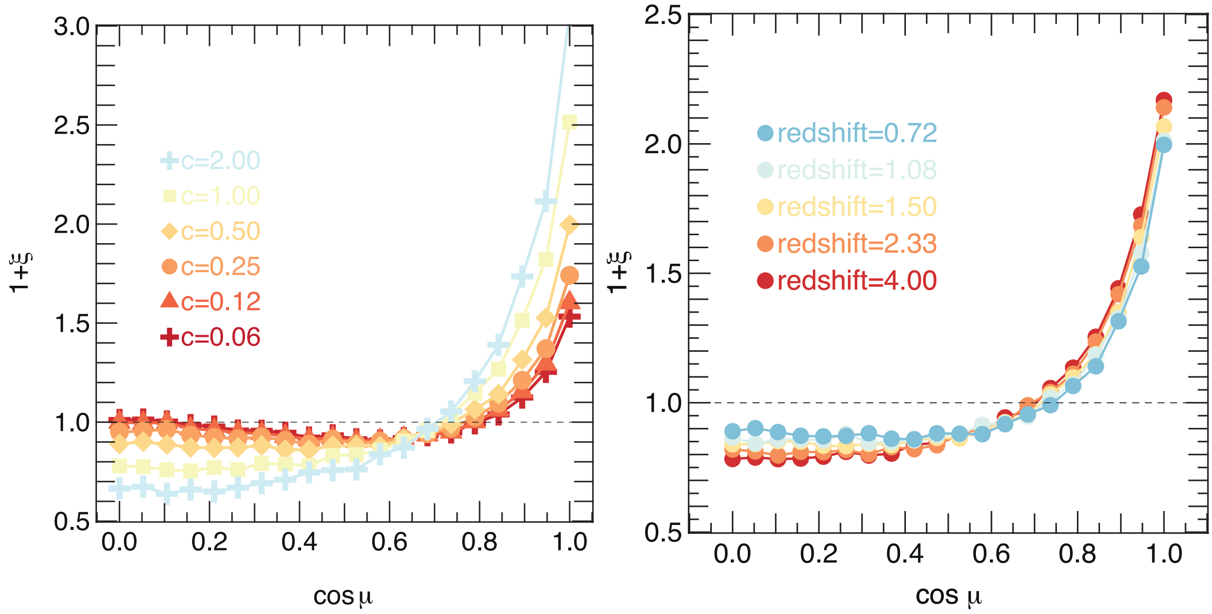

Figure B1. *Left* The probability distribution of the cosine of the angle between the vorticity and the direction of the filament measured in $\mathcal{S}_{20}^{\rm cool}(z=0.7)$ for different persistence threshold. The level of persistence of the main text corresponds to $c=0.5$. *Right* The probability distribution of the cosine of the angle between the vorticity and the direction of the skeleton, measured in $\mathcal{S}_{20}^{\rm cool}(0.7)$ for various redshifts as labeled. The amplitude of the correlation decreases with cosmic time.

filaments as a function of the persistence level for a range of values. The alignment is strongest with the largest scale filamentary structure corresponding to the least dynamically evolved features of the field. Here the gas density was sampled over a cube of size 512^3. It was then smoothed over 8 pixels (300 kpc) and the persistent skeleton was computed from the logarithm of that smoothed field normalized to its standard deviation. Hence the persistence levels 0.06, 0.12... to 2 are in units of this root mean square.

Fig. B2 gives visual impression of the corresponding structure of the skeleton as a function of these persistence levels: the skeleton has a tree-like structure, for which each level of lower persistence contributes smaller branches. Hence the persistence level of 0.5 used in the main text corresponds to a description of the main filaments of the simulation.

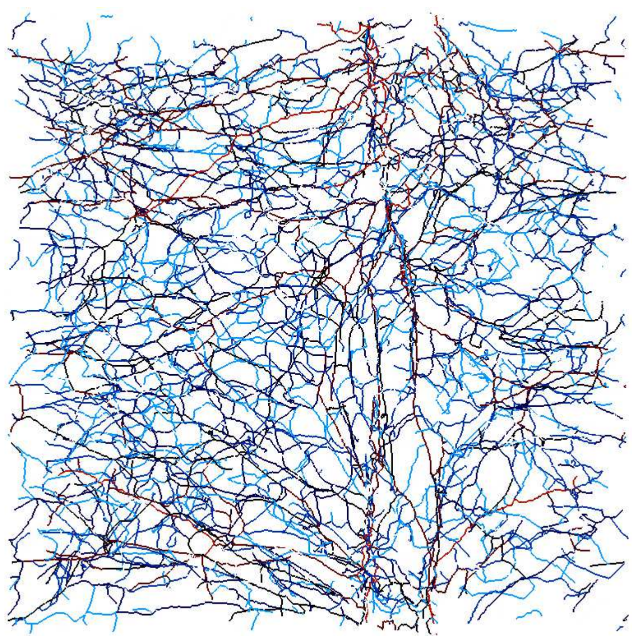

Figure B2. The skeleton measured in $\mathcal{S}_{20}^{\rm cool}(0.7)$ for increasing persistence threshold, 0.06, 0.12... to 2, from light blue to red; the skeleton has tree-like structure where the main branches correspond to the most persistent ones. The level of persistence of the main text corresponds to the dark blue and red branches.

APPENDIX C: TIDAL FIELD-VORTICITY ALIGNMENT

Fig. C1 displays the probability distribution of the cosine of the angle between the vorticity and the eigenvectors of the tidal field tensor, $\cos\gamma$. The vorticity tends to be perpendicular to the minor axis (e_3) of the tidal tensor which corresponds to the axis along which material is collapsing fastest. It is qualitatively in agreement with Fig. 2 and with Libeskind et al. (2013) which focus respectively on the eigenvectors of the hessian of the density, and the eigenvectors of the shear tensor. For the latter, the description is kinematic, rather than dynamical for the tidal field.

APPENDIX D: ZOOLOGY OF CAUSTICS

Fig. D1 shows a bundle of cross sections of vorticity computed as in Fig. 3.

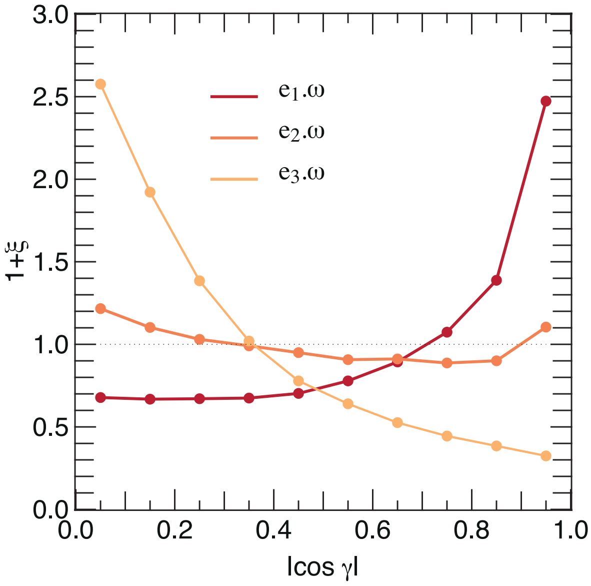

Figure C1. The probability distribution of the cosine of the angle between the vorticity and the eigenvectors of the tidal tensor, measured in $\mathcal{S}_{100}^{\rm CDM}$. The vorticity tends to be perpendicular to the minor axis (e_3) of the tidal tensor: the excess of probability to have $|\cos\theta|$ in $[0, 0.5]$ (that is $60 \leqslant \theta \leqslant 90^{\rm o}$) is 50 per cent relative to random orientations. The vorticity tends also to be aligned with the major axis (e_1): the excess probability to have $|\cos\theta|$ in $[0.5, 1]$ (that is $0 \leqslant \theta \leqslant 60^{\rm o}$) is 25 per cent relative to random orientations. e_3 corresponds to the axis along which material is collapsing fastest.

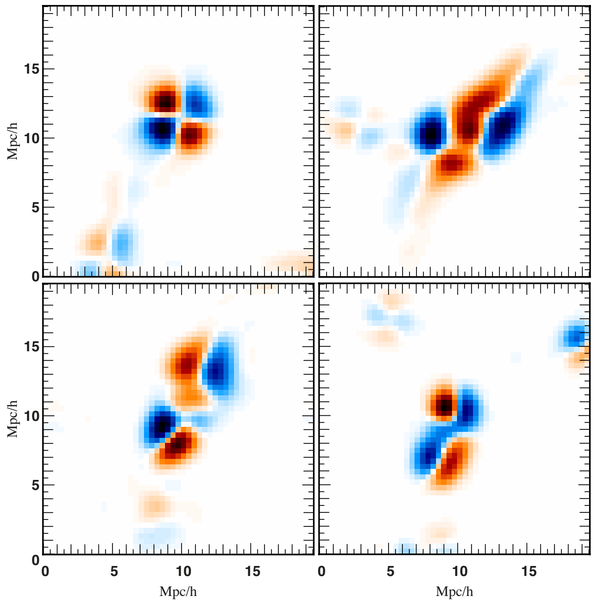

Figure D1. different kinds of vorticity cross sections.

APPENDIX E: DEFINING ZERO VORTICITY

The algorithm `DisPerSE` introduced by Sousbie (2011) is used to defined the density walls and the contours of minimal vorticity. The density walls are computed as being the ascending 2-manifolds of the skeleton calculated on the density field. The contours of minimal vorticity are defined as being the descending 2-manifolds of the skeleton calculated on the norm of the vorticity field. Since the vorticity is really well defined only on the neighbourhood of caustics, a mask is applied when the walls are computed, which covers all the regions of space where the density is lower than 10 per cent of the maximum density and the vorticity lower than 10 per cent of the maximum vorticity. The results of the computation of the density walls and minimal vorticity contours are tessellations, which means sets of triangles. For each triangle in the minimal vorticity tessellation we find its nearest neighbours in the density tessellation. Smoothing is achieved by averaging the position of each vertex with that of its direct neighbours. A smoothing coefficient S =N means that this operation is repeated N times. The cosine between the normals of both triangles is then calculated.